ACS APPLIED MATERIALS & INTERFACES

Research Article

www.acsami.org

Controlling the Texture and Crystallinity of Evaporated Lead Phthalocyanine Thin Films for Near-Infrared Sensitive Solar Cells

Karolien Vasseur,[†,‡] Katharina Broch,[§] Alexander L. Ayzner,[⊥] Barry P. Rand,[†] David Cheyns,[*,†] Christian Frank,[§] Frank Schreiber,[§] Michael F. Toney,[⊥] Ludo Froyen,[‡] and Paul Heremans[†,#]

[†]imec, Kapeldreef 75, 3001 Heverlee, Belgium

[‡]Department of Metallurgy and Materials Engineering, KU Leuven, Kasteelpark Arenberg 44, 3001 Heverlee, Belgium

[§]Institut für Angewandte Physik and LISA +, Universität Tübingen, Auf der Morgenstelle 10, Tübingen 72076, Germany

[⊥]Stanford Synchrotron Radiation Lightsource, SLAC National Accelerator Laboratory, Menlo Park, California 94025, United States

[#]Department of Electrical Engineering, KU Leuven, Kasteelpark Arenberg 10, B-3001 Heverlee, Belgium

Supporting Information

ABSTRACT: To achieve organic solar cells with a broadened spectral absorption, we aim to promote the growth of the near-infrared (NIR)-active polymorph of lead phthalocyanine (PbPc) on a relevant electrode for solar cell applications. We studied the effect of different substrate modification layers on PbPc thin film structure as a function of thickness and deposition rate (r_{dep}). We characterized crystallinity and orientation by grazing incidence X-ray diffraction (GIXD) and in situ X-ray reflectivity (XRR) and correlated these data to the performance of bilayer solar cells. When deposited onto a self-assembled monolayer (SAM) or a molybdenum oxide (MoO_3) buffer layer, the crystallinity of the PbPc films improves with thickness. The transition from a partially crystalline layer close to the substrate to a more crystalline film with a higher content of the NIR-active phase is enhanced at low r_{dep}, thereby leading to solar cells that exhibit a higher maximum in short circuit current density (J_{SC}) for thinner donor layers. The insertion of a CuI layer induces the formation of strongly textured, crystalline PbPc layers with a vertically homogeneous structure. Solar cells based on these templated donor layers show a variation of J_{SC} with thickness that is independent of r_{dep}. Consequently, without decreasing r_{dep} we could achieve J_{SC} = 10 mA/cm^2, yielding a bilayer solar cell with a peak external quantum efficiency (EQE) of 35% at 900 nm, and an overall power conversion efficiency (PCE) of 2.9%.

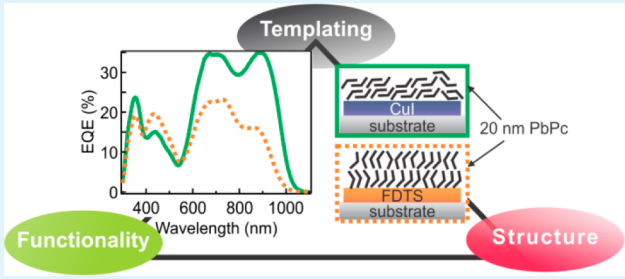

KEYWORDS: *structural templating, molecular orientation, polymorphism, copper iodide (CuI), self-assembled monolayer (SAM), planar heterojunction*

1. INTRODUCTION

Continuous progress in designing new organic semiconductors,[1−3] optimizing device architectures,[4,5] and controlling active layer morphology[6−10] has allowed organic solar cell efficiencies to improve dramatically, with record efficiencies now exceeding 10%.[11] Further improvement of efficiency requires an increased overlap with the solar spectrum in order to maximize photocurrent generation, and in particular, for use with complementary absorbing tandem cells.[12] Since an important part of the photon flux is situated above λ = 800 nm, it is key to incorporate organic solar cells into the tandem structure that exhibit a sensitivity into the near-infrared (NIR) region while simultaneously ensuring efficient photon-to-current conversion.

Among small-molecular-weight donor materials, phthalocyanines (Pcs) are an archetypal material class due to their high optical absorption coefficients in the visible region and their tunable functional properties by incorporating different metal ions in the Pc ring.[13] Introducing a large metal ion, a metal-halide or metal-oxo moiety into the Pc ring disrupts its planarity; the three-dimensionality of the resultant molecule causes its optical and electrical properties in the solid state to be strongly influenced by molecular packing.[14−19] Nonplanar Pcs such as titanyl (TiOPc),[4,20−22] vanadyl (VOPc)[23] and lead Pc (PbPc)[24,25] are reported to crystallize as a variety of polymorphs, most of them exhibiting either monoclinic or triclinic symmetry. The triclinic polymorph of these compounds displays a broadened and red-shifted absorption spectrum due to the increased intermolecular interactions in this close packing arrangement.[10] For PbPc, the phase transition from monoclinic to triclinic is accompanied by a distinct shift of the dominant peak in the absorption spectrum from λ = 740 nm to λ = 900 nm.[26−28] The characteristic absorption peak of triclinic PbPc is positioned at even longer

Received: May 21, 2013
Accepted: August 1, 2013
Published: August 1, 2013

wavelengths than that of the NIR absorbing phase of TiOPc and ClAlPc, rendering PbPc a promising candidate to achieve high-performance NIR-sensitive solar cells.

Promoting the growth of the triclinic polymorph for fabricating solar cells with NIR sensitivity requires insight into the thin film structure of nonplanar Pcs. Processing parameters enabling structural control include (i) growth conditions, including substrate temperature, deposition rate (r_{dep}) and the substrate, and (ii) postdeposition treatments such as thermal and solvent annealing. For PbPc, the monoclinic to triclinic phase transition has been achieved by thermal annealing[29] and applying high pressure[30] on the as-deposited film. The growth of the triclinic polymorph was enhanced by increasing the substrate temperature and decreasing r_{dep}.[15,31] Our previous study on PbPc films grown on ITO substrates indicated an evolving structure with thickness that was shown to sensitively depend upon r_{dep} and substrate temperature. There, the short-circuit current density (J_{SC}) of planar PbPc/C_{60} solar cells amounted to 8.5 mA/cm^2, but this value remains limited by the fact that the exciton diffusion length of PbPc was less than the film thickness needed to reach such J_{SC} values (12 nm vs 40 nm, respectively).[32] In order to limit the parasitic absorption of the poorly ordered PbPc layer formed close to the ITO substrate, the formation of the triclinic phase near the substrate surface should be enhanced during the early stages of thin film growth. Consequently, the optimum in the photocurrent will shift to thinner donor layers, which should result in solar cells with higher performance.

As the growth of an organic layer is governed by the delicate balance between molecule−substrate and molecule−molecule interactions,[33] modification of the substrate surface properties is an effective way to change the organic thin film structure, including crystallinity, crystal phase, and molecular orientation.[34−38] The insertion of a pentacene, sexithiophene, para-sexiphenyl, CuPc or ZnPc layer between the ITO substrate and the PbPc thin film has proven to promote the formation of the triclinic phase.[39−42] Besides organic templating layers, CuI has recently been demonstrated to efficiently template PbPc layers. Shim et al.[43,44] reported on PbPc solar cells with a CuI interlayer achieving an increased J_{SC} up to 8.7 mA/cm^2. This improvement is mainly ascribed to the increased crystallinity and texturing of the PbPc layer. The templating effect of CuI was also demonstrated for CuPc,[45] ZnPc,[6] and TiOPc[46] layers, where the molecular orientation changed from edge-on to face-on upon the insertion of CuI. This orientation change has a complex effect on the resulting device performance, which is described for planar ZnPc/C_{60} heterojunction (HJ) solar cells by Rand et al.[6]

Other surface modifications that have been investigated for solar cell applications include self-assembled monolayers (SAMs)[47−52] and metal oxide layers.[53,54] Although it is well-known that SAMs induce an edge-on orientation of Pcs,[55,56] the main goal of inserting these layers has been to control the work function of the anode rather than to template the donor layer that is deposited on top. Recently, however, a SAM of 1H,1H,2H,2H-perfluorodecyltrichlorosilane (FDTS) was shown to exhibit a strong templating effect on ClAlPc layers, and this resulted in planar solar cells with significantly improved efficiencies.[5]

As the performance of OPV cells critically relies on the morphology and crystalline structure of the thin films involved, a thorough study of the structure−property relationship of the donor layer as well as insight into parameters that control thin film structure is needed to further improve solar cell efficiency.[57,58] In this work, we compare the influence of various surface modification layers, namely FDTS, CuI and MoO_3 as a reference, on the structural evolution of PbPc thin films when deposited at two different r_{dep}, with the aim to fabricate efficient NIR-sensitive solar cells. The structure of the PbPc thin films is elucidated by investigating their crystallinity and preferred orientation, which is referred to as texture. This is done by correlating optical absorption spectroscopy measurements with structural information obtained by in situ out-of-plane Bragg diffraction to probe the vertical ordering and two-dimensional grazing incidence X-ray diffraction (2D GIXD)[59−62] that reveal the in-plane ordering. Finally, we investigate the consequences of the PbPc donor layer structure and crystallinity on the spectral response in planar HJ solar cells.

2. EXPERIMENTAL METHODS

2.1. Substrate Preparation and Thin Film Deposition. The substrates used in this study are glass substrates with 110 nm thick prepatterned indium−tin-oxide (ITO, Kintec) and highly doped n^{+2}-type silicon wafers with thermally grown SiO_2. Substrate cleaning consisted of sonication in detergent, deionized water and acetone, followed by submersion in hot isopropanol. Finally, a 15 min ultraviolet-O_3 treatment was applied.

The growth of PbPc is studied on three different surfaces: on top of (i) MoO_3, (ii) FDTS, or (iii) CuI, grown on glass/ITO or SiO_2. The MoO_3 layer of 2 nm thickness is evaporated at a rate of 1 Å/s in a high vacuum evaporator with a base pressure $\approx 1 \times 10^{-7}$ Torr. A 1 nm thick layer of CuI is deposited in the same system at a rate of 0.2 Å/s, whereas FDTS is applied by vapor phase deposition in a home-built oven at 140 °C under reduced pressure.

The organic materials, PbPc (Sigma-Aldrich), fullerene (C_{60}, SES research), and bathocuproine (BCP, Sigma-Aldrich) were purified once using gradient sublimation, while Ag, CuI and MoO_3 were used as received. Organic thin films were deposited by thermal evaporation in a high vacuum evaporator with a base pressure $\approx 1 \times 10^{-7}$ Torr, and the substrate temperature was fixed to room temperature. The PbPc films have been evaporated at r_{dep} = 0.05 or r_{dep} = 1 Å/s, as monitored by a quartz crystal microbalance (QCM). Note: The thickness of PbPc on CuI was systematically 80% of the thickness of PbPc deposited on MoO_3, FDTS, or ITO, as determined by ellipsometry, and was accounted for in the thicknesses deposited. For solar cell structures, subsequent organic layers were deposited at r_{dep} = 1 Å/s in the same system without breaking vacuum. The 120 nm thick Ag cathode is evaporated through a shadow mask, defining an active area of 0.134 cm^2.

2.2. Thin Film Characterization (postgrowth). Absorption spectra of the PbPc films on glass covered with MoO_3, CuI, or FDTS were measured between 300 and 1100 nm with a Shimadzu UV-1601PC UV−visible spectrophotometer.

Grazing incidence X-ray diffraction (GIXD) spectra were acquired on PbPc films deposited at r_{dep} = 0.05 Å s^{-1} and r_{dep} = 1 Å/s on SiO_2 substrates coated with either MoO_3, FDTS, or CuI. The use of SiO_2 substrates for structural analysis instead of ITO substrates is motivated by the roughness of commercially available ITO covered glass slides which limits the signal-to-background ratio in X-ray diffraction (XRD) measurements. However, to correlate PbPc thin film structure with the performance of solar cells in which the donor layer is deposited onto an untreated ITO anode, the structural evolution of PbPc on ITO is also of interest. We mimic this case by depositing a 2 nm-thick MoO_3 layer on top of the SiO_2 substrate, assuming that the PbPc thin film structure on ITO and MoO_3 is qualitatively similar, although not quantitatively identical. We support this assumption by two observations: (i) ITO and MoO_3 have an equal surface enthalpy as determined by static contact angle measurements and (ii) solar cells with and without MoO_3 anode buffer layer display similar external

quantum efficiency (EQE) spectra as shown in Figure S1 available in the Supporting Information, thus indicating that both PbPc donor layers exhibit a similar structure.

The GIXD measurements were performed at the Stanford Synchrotron Radiation Lightsource (SSRL) beamline 11−3 with an X-ray wavelength of 0.976 Å and an area detector (MAR345). First, an incidence angle of $\varphi = 0.12°$ slightly above the critical angle of the films ($\theta_c = 0.116°$) was chosen. Second, an incidence angle of $\varphi = 0.08°$ was used to probe the near-surface structure (∼5−10 nm) of the films. Typical exposure times were 120 s. The resolution of the GIXD data obtained using the image plate detector is determined by the sample size (12.5 × 12.5 mm), the distance between the sample and the detector as determined by calibration (38.6 cm), and the detector pixel size (150 × 150 μm^2). The overall resolution of the GIXD measurements is about 0.05−0.1 $Å^{-1}$. To prevent beam damage, we performed measurements under a He atmosphere. The sample−detector distance was calibrated using a LaB_6 standard.

The GIXD measurements were analyzed using the software package WxDiff, provided by Dr. Stefan Mannsfeld.[63] Diffraction patterns are distortion corrected (θ-dependent image distortion introduced by planar detector surface) before performing the quantitative analysis on the images. Background correction is also applied when diffraction peak intensities are calculated. The GIXD data are expressed as a function of the scattering vector q

$$q = \sqrt{(q_{xy}^{\ 2} + q_z^{\ 2})} \tag{1}$$

The polar angle χ equals 0° at $q_{xy} = 0$ and is 90° at $q_z = 0$. For diffraction peaks $q = 0.53$ $Å^{-1}$ and $q = 0.9$ $Å^{-1}$, the intensity profile I_q is obtained as a function of χ

$$\text{for } \varphi = 0.12°: I_q(\chi) = \frac{1}{t}\int_{q_1}^{q_2} I(\chi, q)dq \tag{2}$$

$$\text{for } \varphi = 0.08°: I_q(\chi) = \int_{q_1}^{q_2} I(\chi, q)dq \tag{3}$$

with t the PbPc film thickness. The integral in eqs 2 and 3 is approximated by summing intensities over an arc segment Δq that is chosen to encompass the entire peak and roughly corresponds to q ± 0.08 $Å^{-1}$.

Figure S2 provides a schematic on the GIXD data treatment explained here. Previous experiments have shown that the error on the calculated $I_q(\chi)$ value is about 10%.[64] From $I_q(\chi)$, the degree of crystallinity (doc) is calculated as follows:

$$\text{doc} = q\int_0^{\pi/2} I_q(\chi)\sin(\chi)d\chi \tag{4}$$

2.3. In Situ X-ray Reflectivity Measurements. To complement the 2D GIXD measurements that give information about the in-plane structure, we performed in situ X-ray reflectivity (XRR) measurements to study the out-of-plane structure of the PbPc films. The PbPc thin films are deposited in a portable ultrahigh vacuum chamber with a Be window that enables in situ XRD measurements,[65] the unique capabilities of which are demonstrated in ref 66−68. The pressure during deposition was ∼1×10^{-7} Torr, and PbPc was deposited at r_{dep} = 0.05 Å/s as monitored by a QCM. Similar substrates as for the 2D GIXD measurements were employed. Following the evolution of the first order Bragg peak in real-time was hindered due to the chosen deposition rate limiting the integration time, and hence the temporal resolution of the measurement. Therefore, we opted for in situ but not real-time XRR measurements which are performed by interrupting PbPc deposition after the growth of a 10 nm-thick PbPc adlayer. We proceeded with the depositions and subsequent XRR measurements until a final PbPc layer thickness of 60 nm was achieved. We confirmed that the structure of the final PbPc layer of 60 nm thickness was similar after a continuous and an interrupted growth process, as is shown in Figure S3 in the Supporting Information.

The XRR measurements were performed on a GE XRD 3003TT diffractometer using Cu Kα radiation and a double-bounce (compressor) monochromator combined with multilayer optics. An integration time of 30 s per 0.02° was used for scanning $\theta/2\theta$.

2.4. Solar Cell Characterization. Current density−voltage characteristics of photovoltaic cells were measured in dark and under simulated solar light, using a Keithley 2602 in combination with an Abet solar simulator, calibrated to produce 100 mW/cm^2 AM1.5G illumination. In the EQE setup, light from Xe and quartz halogen lamps were coupled into a monochromator and their intensities calibrated with a Si photodiode. The light incident on the device was chopped and the modulated current signal detected with current−voltage and lock-in amplifiers.

3. RESULTS

3.1. Thin Film Absorption. Optical absorption measurements were performed to study the evolution in the structure of the PbPc layer as a function of layer thickness, deposition rate and templating layer. These data are relevant for determining the PbPc structure, as the triclinic phase is reported to have an absorption spectrum that strongly differs from the monoclinic absorption spectrum.[15] The latter is characterized by a doublet in the Q-band at λ = 670 nm and λ = 740 nm. The molecular packing in the triclinic unit cell leads to the appearance of additional oscillator strength on the red side of the absorption spectrum, at λ = 900 nm. This feature is likely due to enhanced intermolecular interaction associated with this solid state packing arrangement.[10] The absorption spectrum of an amorphous film was reported to be identical to that of the monoclinic phase,[28] which can be explained by the weaker intermolecular interaction in the monoclinic packing structure.

Figure 1 depicts absorption spectra of PbPc films with thicknesses of 20, 40, and 60 nm deposited at r_{dep} = 0.05 and 1 Å/s onto glass substrates coated with MoO_3, FDTS, or CuI. For the PbPc films deposited at r_{dep} = 1 Å/s onto MoO_3 (Figure 1 a), the dominant absorption peak is situated at λ = 740 nm for all films. With increasing thickness, the peak corresponding to the absorption of the triclinic phase emerges around λ = 900 nm and increases faster than the peak at λ = 740 nm. For films grown at r_{dep} = 0.05 Å/s, the NIR peak is already distinguishable for the thinnest layer and its intensity increase with thickness is more pronounced than for r_{dep} = 1 Å/s. These observations suggest a structural evolution with thickness that is influenced by the deposition conditions. A similar trend with film thickness can be observed in PbPc films deposited on FDTS treated substrates (Figure 1 b), although the 20 nm thick film deposited at low r_{dep} exhibits a significantly decreased absorption peak at λ = 740 nm. On CuI (Figure 1c), only a small dependence on r_{dep} is apparent, although films deposited at 1 Å/s exhibit a slightly higher absorption intensity at λ = 740 nm compared to films deposited at 0.05 Å/s. The latter films display an absorption spectrum that is commensurate with that of the triclinic polymorph, namely the peak at λ = 900 nm is significantly more intense than the doublet, the dominant peak of which has shifted from λ = 740 nm to λ = 728 nm. In contrast to PbPc films grown on MoO_3 and FDTS, the relative peak intensities in the absorption spectrum of PbPc on CuI are almost independent of thickness, and this indicates little to no structural evolution in these films.

3.2. X-ray Diffraction Measurements. To further investigate the structural evolution of PbPc thin films and its dependence on the substrate as observed in optical absorption measurements, we performed XRD measurements on the various PbPc layers. First, the out-of-plane ordering is probed with specular scans shown in Figure 2. These measurements were performed in situ for PbPc films deposited at r_{dep} = 0.05

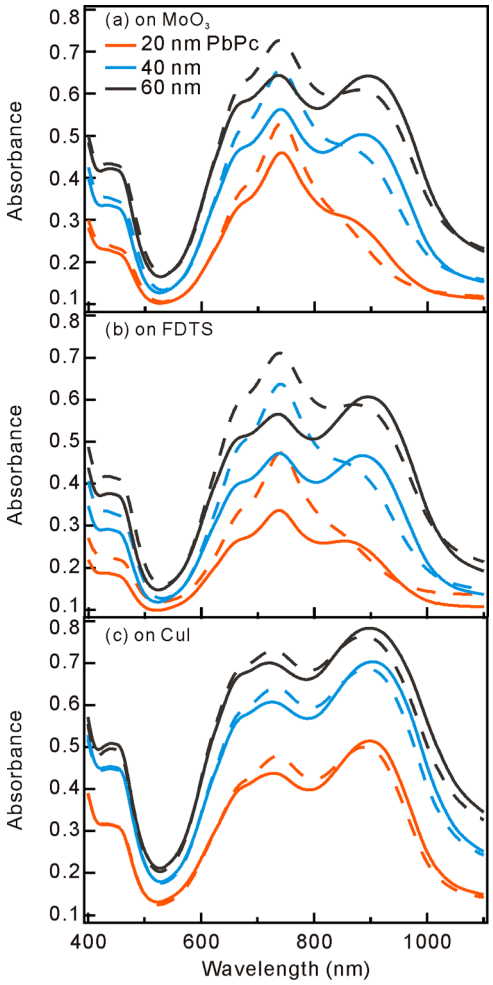

Figure 1. Absorption spectra for PbPc films of varying thickness grown on top of glass substrates with different surface modification layers: (a) MoO_3, (b) FDTS, (c) CuI. The dashed lines correspond to PbPc films grown at r_{dep} = 1 Å/s, whereas the solid lines refer to films grown at r_{dep} = 0.05 Å/s.

Å/s onto SiO_2 substrates coated with different templating layers. Using FDTS, the PbPc layers exhibit Bragg peaks at q_z = 0.49 $Å^{-1}$ and q_z = 0.53 $Å^{-1}$, the relative intensities of which change with thickness. The broad Bragg peak at q_z = 0.49 $Å^{-1}$ changes very little, but with increasing film thickness a second and narrower Bragg peak emerges at q_z = 0.53 $Å^{-1}$, pointing to the nucleation of larger crystallites in the out-of-plane direction, that have a different crystal structure or another orientation with respect to the substrate surface. Because of close, or sometimes even overlapping, peak positions of the monoclinic[13] (M) and triclinic[14] (T) structure, peak indexing is nontrivial and remains rather speculative. On the basis of the peak positions, the Bragg peak at q_z = 0.49 $Å^{-1}$ corresponds to an interplanar distance d = 12.8 Å and can be assigned to T (0 0 1) or M (2 0 0), whereas the peak at q_z = 0.53 $Å^{-1}$ (d = 11.9 Å) originates from the triclinic phase but from the (1 0 0) or (1 −1 0) diffracting plane. The out-of-plane structure of PbPc films grown on a MoO_3 buffer layer is similar to that on FDTS, namely two diffraction peaks can be discerned from which the peak at q_z = 0.53 $Å^{-1}$ increases with PbPc thickness. It should be noted that the determination of accurate peak positions and intensities is complicated by the apparent peak shift with thickness. This could be caused by the changing interference

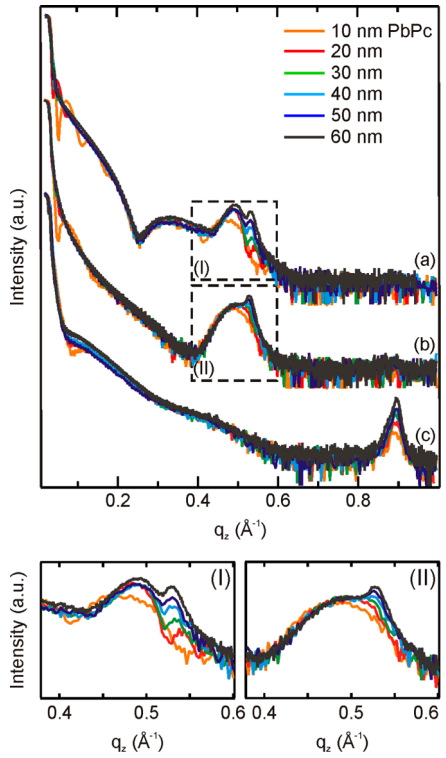

Figure 2. In situ XRR measurements (normalized data) performed after the subsequent deposition of PbPc adlayers of 10 nm thickness, deposited at 0.05 Å/s onto SiO_2 substrates covered with (a) MoO_3, (b) FDTS, (c) CuI. A zoom-in of the Bragg peaks on MoO_3 (I) and FDTS (II) is shown below.

between the smooth MoO_3 layer and the overlaying PbPc film (i.e., a different relative amplitude of the individual scattering contributions[36,46]) or the finite-size induced strain in the PbPc film. On CuI, PbPc layers display a dramatically different vertical ordering, evidenced by the presence of a different, sharp Bragg peak at q_z = 0.90 $Å^{-1}$. This peak shows little evolution with thickness (consistent with the absorption data), and indicates a periodic structure normal to the substrate with an interplanar distance of d = 7 Å. A close value, d = 7.07 Å corresponds to the M (3 2 0) diffraction.[13]

For the 60 nm thick films, rocking curves have been measured on the Bragg peaks in Figure 2 and are plotted in Figure S4, available in the Supporting Information. Both on FDTS and MoO_3, the full width half-maximum (fwhm) of the rocking curve around q_z = 0.49 $Å^{-1}$ is 0.04° (with a low baseline intensity), meaning that these crystallites exhibit a very low mosaicity on both substrates. The rocking curve around q_z = 0.53 $Å^{-1}$ on FDTS on the one hand, consists of a peak with a fwhm of 0.04° superimposed on a nonzero baseline indicating the coexistence of well-oriented and disordered misoriented crystallites. On MoO_3 on the other hand, only a large baseline is present which indicates a population of crystallites with a large mosaicity diffracting at q_z = 0.53 $Å^{-1}$.

To complement the information regarding vertical ordering of PbPc thin films, we have used 2D GIXD to sample a large fraction of the reciprocal space in a rapid fashion. In Figure 3, 2D GIXD patterns acquired on 20 and 60 nm thick PbPc films deposited onto the three different templating layers are shown. When comparing the structure of PbPc films with the same thickness on different substrates (Figure 3, top and bottom rows), important structural differences can be observed. On

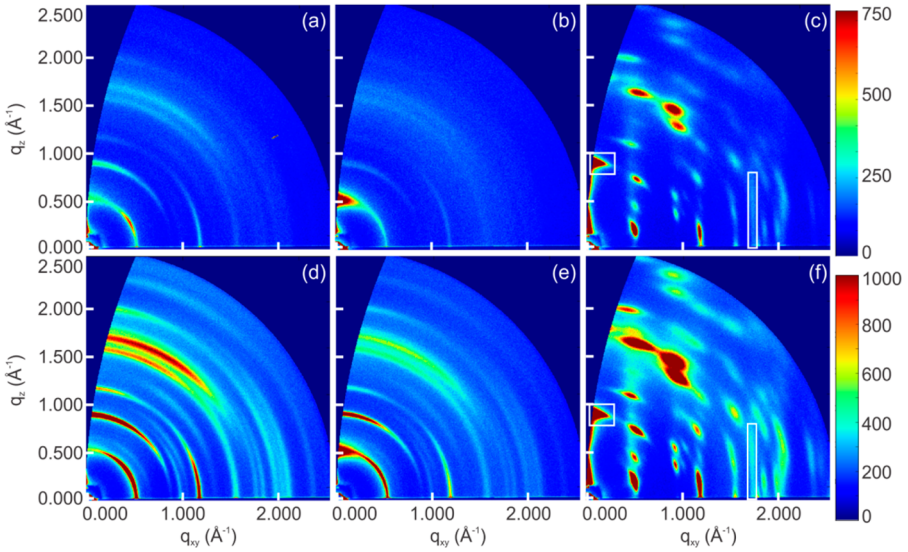

Figure 3. Grazing incidence X-ray diffraction with an area detector (2D GIXD) on PbPc layers with a thickness of (a–c) 20 and (d–f) 60 nm. These layers are deposited on SiO_2 substrates at 0.05 Å/s with three different buffer layers: (a, d) MoO_3, (b, e) FDTS, (c, f) CuI. The areas in c and f in boxes indicate the position of CuI diffraction peaks.

MoO_3 and FDTS, similar (arched) diffraction peaks occur, albeit with different preferential orientations and relative intensities. On the CuI substrate, the presence of multiple diffraction spots points to highly crystalline and strongly textured PbPc films where only the intensities increase as the film thickens (no change in texture with thickness). When considering the 2D GIXD patterns of the PbPc films on the MoO_3 and FDTS substrates, the previously observed diffraction peaks at q_z = 0.49 Å^{-1} and q_z = 0.53 Å^{-1} are indiscernible due to the limited resolution of the GIXD setup. When studying the convoluted peak around q = 0.53 Å^{-1} (cfr. eq 1) in more detail, a markedly different preferential orientation of PbPc crystallites on the FDTS-modified substrate compared to that on MoO_3 is apparent, which is quantified with pole figures.

In Figure 4, we show the (thickness normalized) pole figures $I_q(\chi)$ of the diffraction peaks at q = 0.53 Å^{-1} (cfr. eqs 1 and 2) for PbPc films on MoO_3 and FDTS. At φ = 0.12° (Figure 4 a), in essence the bulk structure of the PbPc films on FDTS is probed, and the maximal intensity of the diffraction peak occurs near $\chi \approx 0°$ (recall that the GIXD geometry prevents data for $\chi \leq 2–3°$[37]). This maximum intensity ($\chi \approx 0°$) decreases with thickness, whereas the intensity at $\chi \approx 58°$ increases, thereby showing a change in the preferred orientation of the PbPc crystals. At a small incident angle of φ = 0.08°, the X-rays preferentially probe the near-surface structure of the PbPc films. As can been seen in Figure 4 b, there is no change in texture with thickness beyond t > 30 nm; the top structure of 30 nm thick PbPc films exhibits its only intensity maximum at $\chi \approx 58°$. This demonstrates that the plane diffracting at q = 0.53 Å^{-1} reorients (the crystallites change preferred orientation) from being parallel (at $t \leq 20$ nm) to being tilted at ~58°. On the MoO_3 substrate, this change in preferred orientation with thickness is much less pronounced; the maximum peak intensity along the diffraction arc at q = 0.53 Å^{-1} is near $\chi \approx$ 58° for the thinnest PbPc film (Figure 4 c), and strikingly there is no peak near $\chi \approx 0°$. On the CuI substrate, the diffraction peak at q = 0.53 Å^{-1} is very intense and has a limited angular distribution around $\chi \approx 70°$ demonstrating that PbPc molecules do not change their orientation with thickness. The corresponding (thickness normalized) pole figure $I_q(\chi)$ is

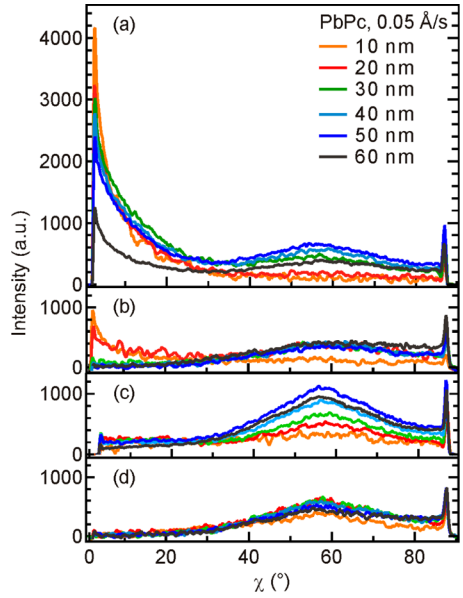

Figure 4. Plot of $I_q(\chi)$, calculated as shown in eqs 1 and 2. The thickness of PbPc layers varies from 10 to 60 nm in steps of 10 nm. Those films were deposited on SiO_2 substrates with (a, b) FDTS or (c, d) MoO_3 as templating layers. Two different incidence angles were used: (a, c) φ = 0.12° and (b, d) φ = 0.08°. Here χ = 0° is normal to the surface, whereas χ = 90° is in-plane.

shown in Figure S5, available in the Supporting Information. In contrast to the PbPc films deposited on MoO_3 and FDTS, the diffraction peak at q = 0.90 Å^{-1} is quite intense, even for the 20 nm thick PbPc layer on CuI. However, the intensity at $q_{xy} \approx 0$ will not be further interpreted, as the CuI substrate exhibits a diffraction peak at q_z = 0.86 Å^{-1} which overlaps with the diffraction from the PbPc film, hindering the analysis.

Comparison of the 2D GIXD patterns for different PbPc film thicknesses reveals an intensity increase for the different diffraction peaks. To quantify this observation, the doc was calculated according to eq 4 and the results are plotted in Figure 5 for diffraction peaks at q = 0.53 Å^{-1} and q = 0.90 Å^{-1}.

dx.doi.org/10.1021/am401933d | ACS Appl. Mater. Interfaces 2013, 5, 8505–8515

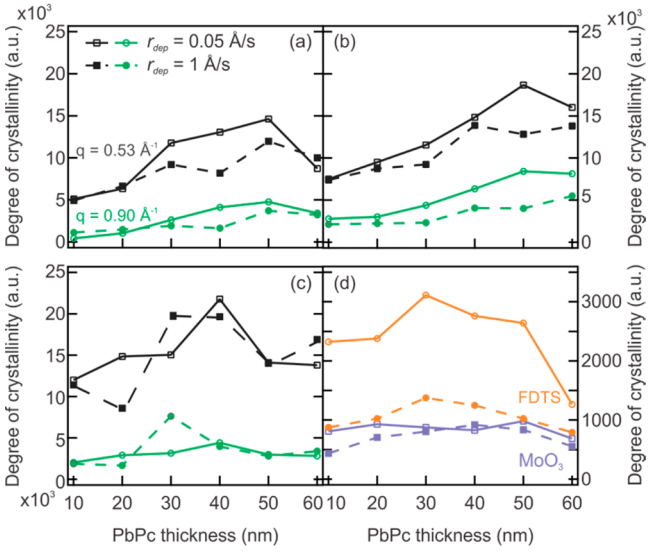

Figure 5. Degree of crystallinity (doc) calculated by eq 4 for diffraction peaks q = 0.53 Å^{-1} and q = 0.90 Å^{-1} and plotted as a function of PbPc layer thickness. PbPc layers are deposited onto (a) FDTS, (b) MoO_3, and (c) CuI. (d) Doc of the diffraction peak at q = 0.53 Å^{-1} calculated for $\chi \approx 0-30°$, to isolate the edge-on oriented PbPc fraction. Solid lines correspond to PbPc films deposited at 1 Å/s, whereas dotted lines correspond to films deposited at 0.05 Å/s.

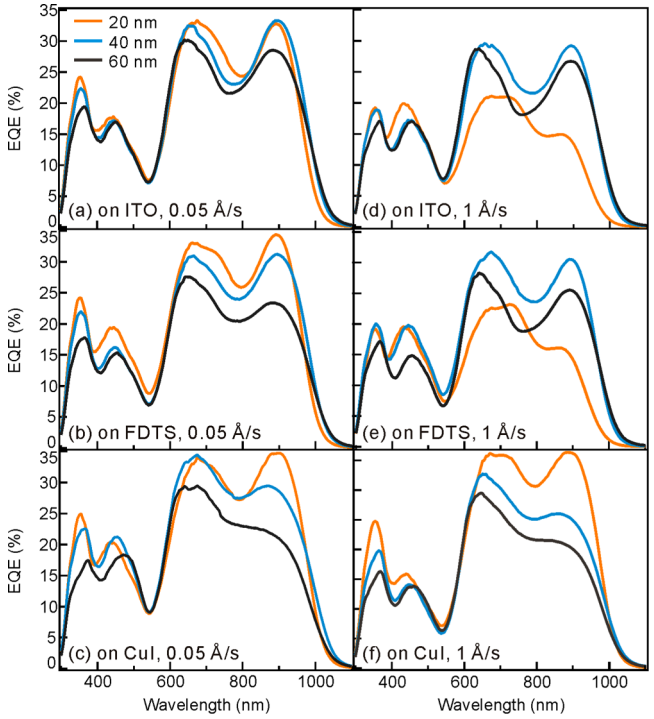

Figure 6. External quantum efficiency (EQE) measurements of solar cells with structure (a) ITO/PbPc (20, 40, 60 nm)/C_{60} (50 nm)/BCP (10 nm)/Ag; (b) FDTS is inserted in between ITO and the PbPc layer, (c) CuI is deposited on top of ITO. In a–c, the PbPc donor layers are deposited at r_{dep} = 0.05 Å/s, whereas in d–f, r_{dep} = 1 Å/s.

Peaks at higher q are not considered in this analysis, as the amount of missing data from polar angles close to χ = 0° becomes too large.[69] On MoO_3 and FDTS, the doc of both diffraction peaks increases with thickness, and this trend is more pronounced at lower r_{dep}. On the CuI substrate, the doc is independent of r_{dep} and of PbPc film thickness. These observations are consistent with the formation of a crystalline PbPc layer that exhibits little structural evolution as a function of film thickness. In Figure 5 d, the doc for the diffraction peak at q = 0.53 Å^{-1} is plotted for χ ranging from ~0 to 30°, in order to isolate the crystallites with this out-of-plane orientation. On FDTS substrates, an important crystalline fraction close to the substrate adopts an out-of-plane orientation when the film is deposited at low r_{dep}. However, at r_{dep} = 1 Å/s, this preferential vertical ordering is less prominent and is comparable to that in films grown on a MoO_3 buffer layer.

3.3. Solar Cell Characterization. To correlate the thin film structure with its photoelectrical properties, we used PbPc films in planar heterojunction solar cells with the following structure: ITO/(FDTS or CuI (1 nm))/PbPc (x nm)/C_{60} (50 nm)/BCP (10 nm)/Ag, where the PbPc layer thickness is varied from 10 to 60 nm in steps of 10 nm. Figure 6 displays the EQE measurements for the solar cells based on a PbPc donor layer deposited at r_{dep} = 0.05 Å/s and r_{dep} = 1 Å/s. In these spectra, the photocurrent contribution from C_{60} occurs at λ = 400–550 nm and from PbPc mainly at λ = 600–1100 nm.

When comparing the solar cells with the PbPc donor layer deposited at low rate (Figure 6a–c), the EQE spectra exhibit the same trend with increasing PbPc layer thickness. The highest photocurrent is measured for the solar cells with 20 nm thick PbPc films. For a 40 nm thick donor layer deposited directly on ITO (Figure 6 a), the peak at λ = 740 nm becomes a dip in the EQE spectrum. When the donor layer thickness is further increased, the EQE decreases over the entire wavelength range. For PbPc grown on FDTS, a similar drop in EQE across all probed excitation wavelengths already occurs from a donor layer thickness of 40 nm onward. On CuI, the evolution of the spectral responsivity as a function of PbPc layer thickness differs in that the peak at λ = 900 nm is reduced first. Solar cells with the thickest donor layers display an overall drop of the EQE signal.

At increased r_{dep} (Figure 6d–f), the evolution of EQE with donor layer thickness is different for solar cells with untreated and FDTS-modified ITO anodes, but not significantly different for solar cells with a CuI layer inserted between ITO and PbPc. In the latter case, the EQE measurements are almost identical for both r_{dep}, hinting toward a similar donor layer structure at both deposition conditions. On ITO substrates with and without FDTS, PbPc layers of 20 nm thickness exhibit a dominant peak in the EQE spectrum at λ = 740 nm. Upon PbPc thickness increase, the dominant peak in the EQE spectrum becomes a dip, whereas the peak at λ = 900 nm undergoes a relatively large increase. For the 60 nm thick donor layers, the EQE signal decreases over the complete wavelength range. When the donor layer is deposited at higher r_{dep} on top of ITO and FDTS, the optimum in the photocurrent is reached for thicker donor layers.

Table 1 summarizes the important device parameters measured under 1 sun AM1.5G illumination on the best performing solar cell for each anode modification. Performance parameters for all fabricated solar cells are assembled in Figure S7 available in the Supporting Information. For solar cells with ITO and FDTS-treated ITO anodes, the evolution of J_{SC} and fill factor (FF) with donor layer thickness is very similar. When the donor layer is deposited at low r_{dep}, J_{SC} peaks at lower PbPc film thickness as was already apparent from EQE measurements. The FF drops with increasing thickness, and this decrease is larger at higher r_{dep}. However, when a CuI

dx.doi.org/10.1021/am401933d | ACS Appl. Mater. Interfaces 2013, 5, 8505–8515

Table 1. Solar Cell Performance Parameters of Best Devices Employing Different Anode Modifications Measured under 1 sun AM1.5G Illumination

device structure	V_{OC} (V)	FF (%)	$J_{SC,EQE}$[a] (mA/cm^2)	PCE[b] (%)
ITO/PbPc (30 nm @ 0.05 Å/s) /C_{60}/BCP/Ag	0.430	54	9.4	2.2
ITO/FDTS/PbPc (30 nm @ 0.05 Å/s)/C_{60}/BCP/Ag	0.450	56	9.5	2.4
ITO/CuI/PbPc (30 nm @ 1 Å/s) /C_{60}/BCP/Ag	0.475	60	10	2.85

[a] $J_{SC,EQE}$ is the J_{SC} expected by integration of the EQE spectrum over the AM1.5G solar spectrum. [b] The PCE is calculated as follows: $J_{SC}V_{OC}$FF/100 mW cm^{-2}

templating layer is used on top of ITO, the growth rate of the donor layer does not affect solar cell performance. Without adapting deposition conditions, J_{SC} could be maximized to 10 mA/cm^2. Compared to a solar cell based on a 30 nm PbPc layer deposited at r_{dep} = 1 Å/s directly onto ITO, this is an increase in photocurrent of more than 50%. In combination with a FF that varies around 60% for all donor layer thicknesses, the insertion of the CuI templating layer resulted in planar PbPc/C_{60} solar cells with a PCE of 2.9%.

4. DISCUSSION

Absorption measurements can be linked to PbPc thin film structure, as the triclinic phase is reported to have an absorption peak at λ = 900 nm, which is significantly red-shifted compared to the main absorption peak in the monoclinic or amorphous spectrum. However, for asymmetrical molecules such as Pcs, molecular orientation can have a significant impact on the absorption strength, which is larger when the transition dipole moment of the molecule (typically in the macrocycle) is aligned with the electric field of the incident light.[25,70] For nonplanar Pcs, the situation is even more complex, as within one unit cell different molecular orientations are present, leading to anisotropic optical properties.[71,72] By modifying the substrate surface, both crystal structure and molecular orientation are changed and significantly affect the optical properties of the thin film.[73,74] Highly interacting surfaces, such as metals or ionic substrates, might induce epitaxial growth of the organic thin film[75] and can even influence the structure of the adsorbed molecules.[76,77] Increasing the film thickness can result in mitigation of such interfacial effects and induce an evolution of structural and optical properties throughout the film.[78]

In our study, in situ XRR and 2D GIXD measurements (cfr. Figures 2 and 3) revealed important changes in the orientation of PbPc crystallites (and molecules) as a function of layer thickness, the templating layer and deposition rate. Furthermore, the 2D GIXD measurements (cfr. Figure 3) and quantitative analysis thereof (cfr. Figure 5) indicate a different volume fraction of crystalline material in the various PbPc films. Although amorphous domains cannot contribute to diffraction peaks, they influence the absorption spectrum at λ = 740 nm. Consequently, the different texture as well as the changing crystallinity of the various PbPc films hinders a quantitative analysis of the absorption measurements, prohibiting an accurate determination of the ratio of the different polymorphs in the films.

Phase identification by means of diffraction measurements is complicated for PbPc films by the similarity of the monoclinic and triclinic unit cell (see Table S2 in the Supporting Information). Moreover, it is very plausible that PbPc can arrange in other crystal structures besides the two polymorphs that are currently described in the literature. For example, Hoshi et al. suggested the growth of another NIR-active PbPc polymorph with an orthorhombic structure on top of KI.[41,79]

Although the measurements performed in this study do not enable an unambiguous identification of the various diffraction peaks and therefore prohibit the quantification of the M/T ratio, the unique combination of spectroscopic and diffraction data on our PbPc films allows us to correlate the texture and crystallinity of the films to their optical and photoelectrical properties. In the following paragraphs, results from spectroscopic and diffraction measurements are discussed side by side in order to determine the structural evolution in PbPc films as a function of the templating layer. Finally, the correlation between the spectral response of planar HJ solar cells and the derived structure of the PbPc donor layers involved is elucidated.

4.1. FDTS. In situ XRR measurements (cfr. Figure 2b) indicate a structural evolution in the PbPc films, as the relative intensities of the diffraction peaks at q_z = 0.49 Å^{-1} and q_z = 0.53 Å^{-1} change with thickness. However, this observation does not prove a phase transition from M to T, as it could also correspond to a change in preferential orientation of the triclinic polymorph. In the 2D GIXD pattern of the PbPc films grown at r_{dep} = 0.05 Å/s (cfr. Figure 3b,e), the convoluted peak at q = 0.53 Å^{-1} displays important changes in the molecular orientation with increasing layer thickness. From the GIXD data analysis (cfr. Figure 4 a and b), it can be seen that this change in preferred orientation occurs when the film thickness is larger than 20 nm. It is plausible that from this thickness onward molecule−molecule interactions dominate the nucleation process instead of molecule−substrate interactions.

Referring back to XRR measurements, the intensity of the peak at q_z = 0.49 Å^{-1} does not change with thickness and the corresponding rocking curve (cfr. Figure S4a in the Supporting Information) indicates that a part of these crystallites have a low mosaicity. The rocking curve around the Bragg peak at q_z = 0.53 Å^{-1} however shows the coexistence of an ordered and disordered fraction of the crystallites. In agreement with the GIXD measurements and a study from Kline et al., we explain this observation by the nucleation of crystallites with a large mosaicity on top of a highly oriented crystallite fraction close to the substrate interface.[80] Taking this into account, it seems a reasonable assumption that the change in texture concerns the diffraction peak at q_z = 0.53 Å^{-1}, which can be assigned to T (1 0 0) or T (1 −1 0). When changing the orientation of the T (1 0 0) or T (1 −1 0) plane with respect to the substrate by rotating the PbPc unit cell clockwise 58° about the c*-axis, the molecular orientation changes on average from significantly edge-on (Pc plane perpendicular to the substrate surface) to almost face-on (Pc plane parallel to the surface). This is schematically illustrated for the T (1 −1 0) plane in Figure S6, available in the Supporting Information.

The structural evolution of the films as a function of thickness illustrates that the nucleation and growth stage is not only governed by thermodynamic processes but also by kinetic considerations. This is further evidenced by the structure of films grown at higher r_{dep}.[21,81] Here, the hypothesized edge-on orientation induced by the substrate is quickly lost. Because of the increased deposition rate, admolecules have less time to arrange in a well-ordered structure. This is not only illustrated

by the difference in texture but also by the limited increase in doc at higher r_{dep} (compared to low r_{dep}).

When we correlate these findings with the optical absorption data while keeping in mind that molecular orientation plays an important role, the absorption spectrum of the 20 nm thick film deposited at r_{dep} = 0.05 Å/s should be quite different from that at r_{dep} = 1 Å/s. Indeed, for the latter film the absorption peak at λ = 740 nm is significantly higher, whereas the NIR absorption peak is lower. The calculated doc of the diffraction peaks at q = 0.53 Å^{-1} and q = 0.90 Å^{-1} is similar and relatively low for both films (cfr. Figure 5a), suggesting that the difference in absorption is mainly induced by the different texture. The low surface energy of FDTS is known to induce an edge-on arrangement of the molecules in order to minimize the substrate-molecule interaction, and this effect is independent of crystallinity or crystal phase.[30] The film close to the substrate has a predominantly amorphous character, as the peak at λ = 740 nm is dominating the absorption spectrum. With increasing thickness, both absorption peaks increase due to a change in the number of molecules adopting a face-on orientation. However, the NIR peak increases much faster, thereby pointing to the enhanced triclinic character of thicker films. As this trend is combined with an increase in doc, the analyzed diffraction peaks at q = 0.53 Å^{-1} and q = 0.90 Å^{-1} must involve the triclinic phase. However, coexistence of monoclinic and triclinic crystallites in the films cannot be excluded. In the films deposited at 1 Å/s, the doc increases at a slower pace. This trend is correlated with a lower absorption peak at λ = 900 nm, again indicating that both diffraction peaks have important triclinic contributions.

By combining all obtained structural data, a schematic of the PbPc film structure as a function of thickness can be drafted and is depicted in Figure 7a. In the first 20 nm close to the substrate, mainly amorphous domains and well-oriented small T and perhaps M crystallites nucleate in which molecules exhibit an edge-on orientation. A larger crystallite density with a larger mean crystalline coherence length nucleates on top of this 20 nm thick well-ordered layer. This results in a less textured layer with on average more molecules adopting a face-on orientation.

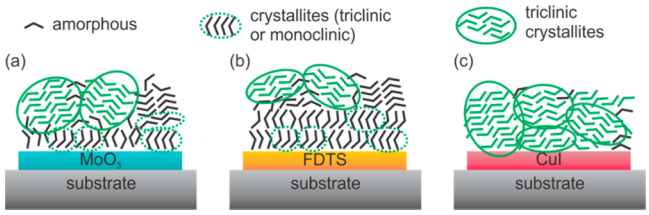

Figure 7. Schematic representations of the PbPc thin film structure, deposited at r_{dep} = 0.05 Å/s on top of substrates modified with (a) FDTS, (b) MoO_3, and (c) CuI.

4.2. MoO_3. The absorption spectra of PbPc films on MoO_3 (cfr. Figure 1a) indicate a structural evolution with increasing layer thickness resembling the evolution in PbPc films deposited on FDTS-modified substrates. For films grown at r_{dep} = 0.05 Å/s, in situ XRR measurements (cfr. Figure 2) and rocking curves of PbPc films are similar for both substrate surfaces. Upon considering in-plane orientations however (cfr. Figure 3 and 4), there is an important difference: on MoO_3 only the first few monolayers of PbPc molecules adopt an edge-on orientation. Beyond a layer thickness of 5−10 nm, the face-on orientation of the molecule is promoted. This translates into higher absorption maxima of PbPc films on MoO_3 compared to on FDTS modified substrates. The higher NIR absorption peak can be attributed to (i) the enhanced face-on orientation of the molecules resulting in an increased absorption strength and (ii) the larger doc for both diffraction peaks at q = 0.53 Å^{-1} and q = 0.90 Å^{-1} compared to the FDTS case.

A schematic of the PbPc film structure is depicted in Figure 7b. Close to the substrate, mainly amorphous domains and some well-oriented small T and perhaps M crystallites nucleate in which molecules exhibit a predominant edge-on orientation. Beyond a film thickness of 5 to 10 nm, more and larger T crystallites nucleate in which molecules predominantly exhibit a face-on orientation.

For layers deposited at r_{dep} = 1 Å/s, the evolution of the absorption spectrum with PbPc layer thickness is almost identical on FDTS and MoO_3. (cfr. Figure 1) The absolute peak heights are slightly higher on MoO_3, which could be explained by the larger amount of face-on oriented PbPc molecules in these films compared to PbPc layers grown on FDTS. Since the molecular orientation almost does not change throughout the film, the increasing NIR absorption peak can directly be correlated to the fraction of triclinic polymorph present. At r_{dep} = 1 Å/s, the NIR-peak as well as the calculated doc is lower than for films deposited at r_{dep} = 0.05 Å/s. Similar to PbPc films grown on FDTS surfaces, the crystallinity and triclinic character of the films decreases upon increasing deposition rate.

4.3. CuI. When studying optical absorption (cfr. Figure 1c), in situ XRR (cfr. Figure 2c) and GIXD measurements (cfr. Figure 3c, f) of PbPc layers deposited on CuI, a limited structural evolution with PbPc thickness is discernible in contrast to the PbPc layers deposited on MoO_3 and FDTS. The PbPc films on CuI display a strong texture and high crystallinity even for the thinnest layers, thereby proving the templating effect of CuI on PbPc.[24] The absorption spectra of the films grown at r_{dep} = 0.05 Å/s are consistent with the absorption of the triclinic polymorph. In situ XRR measurements show only one diffraction peak at q_z = 0.90 Å^{-1}, thereby strongly hinting that this peak originates from a NIR-active phase, in agreement with a publication from Hoshi et al.[41]

In 2D GIXD patterns another diffraction peak, namely at q = 0.53 Å^{-1}, can be observed. It exhibits an exclusively in-plane orientation, thus explaining the absence of this diffraction peak in the XRR measurements. As previously argued for PbPc films grown on FDTS, the in-plane orientation of the diffraction peak at q = 0.53 Å^{-1} corresponds to an increased face-on orientation of PbPc molecules. This implies that for PbPc films grown on CuI, the preferred face-on orientation is preserved throughout the entire film. This observation is in agreement with the distinct face-on orientation of CuPc,[25] ZnPc,[6] and TiOPc[26] when grown on top of CuI.

As a predominantly flat-lying orientation of Pc molecules is beneficial for the absorbance, the highest absorption strengths are obtained for PbPc films on CuI. At r_{dep} = 1 Å/s, the absorption peak at λ = 740 nm is slightly higher compared to the spectra at low r_{dep}. This can either correspond to the promotion of the M phase at increased r_{dep}, or to the decreased overall crystallinity in the film. The doc of the diffraction peaks at q = 0.53 Å^{-1} and q = 0.90 Å^{-1} are similar for both deposition conditions, although it should be noted that for the peak at q = 0.90 Å^{-1} the intensity evolution of the diffraction spot at $q_{xy} \approx 0$ is not considered, which could result in information loss. In

dx.doi.org/10.1021/am401933d | ACS Appl. Mater. Interfaces 2013, 5, 8505−8515

Figure 7c, a schematic illustrates the PbPc thin film structure on a CuI templating layer.

4.4. Solar Cell Performance. Finally, we correlate the structural evolution of the PbPc layers as derived from optical absorption and XRD data to the performance of heterojunction solar cells with the studied PbPc films as donor layers. The spectral response in the solar cells gives information about the exciton harvesting region, which concerns only that part of the PbPc film that extends approximately one exciton diffusion length (L_D) from the donor−acceptor (D−A) interface, whereas with absorption spectroscopy and GIXD the bulk of the PbPc layers is probed. The evolution of the EQE spectra is quite similar for solar cells with FDTS-treated and unmodified ITO anodes. For PbPc donor layers deposited on FDTS and ITO at r_{dep} = 1 Å/s, the EQE spectra reflect the asymmetric layer structure that was already apparent from absorption and XRD data, indicating that the upper part of the layer comprises an increased amount of NIR-active polymorph whereas the film close to the substrate is a mixture of amorphous and small T and perhaps also M domains. This confirms our previous observations on the effect of deposition rate and substrate temperature on the structural evolution of PbPc layers on ITO.[20] In all cases, the contribution of photocurrent by photons absorbed in the C_{60} is low with respect to PbPc. As the reported L_D of C_{60} is approximately 20 nm,[82] the dissociation efficiency of these excitons into free carriers is relatively small.

Solar cells with an untreated or FDTS-modified ITO anode have a maximized performance when the donor layer is deposited at low r_{dep}, which is a condition that promotes the growth of the triclinic polymorph even in the region close to the substrate. The concomitant broadening of the absorption spectrum results in higher photocurrents obtained for thinner films, compared to donor layers deposited at r_{dep} = 1 Å/s. The FF is higher for solar cells with thin PbPc layers, which might be related to the structural inhomogeneity in thicker layers complicating charge transport, and therefore leads to solar cells with a higher PCE. On ITO, the maximum PCE is 2.2%, whereas on FDTS, 2.4% was obtained for donor layers of 30 nm thickness. The corresponding EQE values of these solar cells are over 25% from λ = 610−940 nm, with peak values around 33% at λ = 900 nm.

The spectral response for solar cells based on a donor layer grown on CuI is independent of its deposition rate. The CuI interlayer templates the overlaying PbPc layer by inducing a strong texture and high crystallinity of the predominantly NIR-active phase, irrespective of the applied deposition conditions. Furthermore, the vertical homogeneity and high crystallinity of the PbPc films on CuI can help retaining higher FF up to higher donor layer thicknesses. This means that even without adapting deposition conditions (e.g., at r_{dep} = 1 Å/s) a solar cell with a maximized photocurrent of 10 mA/cm^2 and high FF can be achieved, thereby yielding a PCE of 2.9%. The EQE values of this solar cell are over 30% from λ = 640 to 950 nm with a peak value of over 35% at λ = 900 nm. The maximal photocurrent value obtained on CuI cannot be correlated with an increase in D−A interface area, as the root-mean-square (rms) roughness of PbPc films grown on CuI is smaller than that on ITO and FDTS. This could point to an increased L_D for films deposited on CuI[24] because of an increased excitonic coupling in the π-stacking direction, which might be attributed to the enhanced crystallinity and favorable molecular orientation of those films.[83]

The question remains if the hole transport levels (which are the highest occupied molecular orbitals or HOMO) of the different polymorphs have the same energy. Previous reports have correlated the V_{OC} of OPVs with the HOMO levels of the donor material.[84] As V_{OC} for the different studied devices show only a 50 mV variation, there is an indication that the different polymorphs have related HOMO levels. However, the fact that the devices on ITO or on FDTS have a lower FF indicates a problem with charge extraction, which could be induced by a nonalignment of the transport levels. Detailed transport studies are needed in order to quantify this effect.

5. CONCLUSION

By studying the texture and crystallinity of PbPc layers grown onto a reference oxide layer and two different templating layers, FDTS and CuI, we aimed to gain insight into the structure−property relationship of nonplanar Pcs in order to achieve well-performing NIR-sensitive solar cells. Despite the inability to differentiate between the possible polymorphs present in the films with XRD measurements, the latter allowed us to correlate the texture and crystallinity of the various PbPc layers with their optical properties, as determined by optical absorption measurements and spectral response in bilayer PbPc/C_{60} heterojunction solar cells.

When deposited at low r_{dep} onto FDTS, PbPc molecules arrange in an edge-on configuration up to a film thickness of ∼20 nm. From this point onward, the face-on orientation of PbPc molecules is promoted. At higher r_{dep}, this texturing induced by the low surface energy of FDTS is suppressed. On the MoO_3 substrate, molecules adopt a predominantly face-on orientation from the start. The evolution of the NIR absorption peak at λ = 900 nm is very similar on both substrates, and seems to be correlated to an increase in the doc of the diffraction peaks at q = 0.53 Å^{-1} and q = 0.90 Å^{-1}. The occurrence of a phase transition with increasing film thickness could not be proven by our measurements. The PbPc films deposited onto a CuI templating layer exhibit a strong texture and high crystallinity. The absorption spectra are indicative of an almost exclusively triclinic character of the PbPc films and the absence of structural evolution, irrespective of r_{dep}. Therefore, we can deduce that the diffraction peak at q = 0.90 Å^{-1} must correspond to a NIR-active polymorph, which might have another crystal structure than the triclinic.

In solar cells based on a PbPc donor layer deposited directly on ITO or on ITO modified with FDTS, the maximum in J_{SC} is higher and shifted to thinner donor layers when deposited at low r_{dep}. Notably, a low r_{dep} promotes the transition from a partially crystalline layer close to the substrate to a more crystalline film with a higher proportion of NIR-active phase. Inserting a CuI templating layer between the anode and the PbPc donor layer induced the growth of the NIR-phase from the early stages of film growth and this for both r_{dep}. Despite the increased r_{dep}, a J_{SC} of 10 mA/cm^2 was reached without compromising FF and V_{OC} and resulted in an optimized solar cell with a PCE of 2.9%.

■ ASSOCIATED CONTENT

Supporting Information

The EQE spectra of solar cells with an untreated ITO anode and an anode with MoO_3 buffer layer are compared in Figure S1. Figure S2 provides a schematic on the GIXD data treatment explained in the Experimental Section 2.2. Figure S3 plots in situ XRR data of 60 nm thick PbPc films measured after a

continuous or interrupted deposition process. Rocking curves at diffraction peaks $q = 0.49$ Å^{-1} and $q = 0.53$ Å^{-1}, measured on 60 nm-thick PbPc films grown onto SiO_2 substrates with FDTS and MoO_3 buffer layers are plotted in Figure S4. Figure S5 shows the (thickness normalized) pole figures $I_q(\chi)$ of the diffraction peaks at $q = 0.53$ Å^{-1} (cfr. eqs 1 and 2) for PbPc films deposited on CuI. The change in molecular orientation from the T (1 −1 0) plane is illustrated in Figure S6. Solar cell performance parameters are plotted as a function of donor layer thickness in Figure S7. The AFM images of a representative selection of PbPc films deposited on top of substrates modified with MoO_3, FDTS and CuI layers are shown in Figure S8. In Figure S9, 2D GIXD patterns acquired on 20 nm thick PbPc films deposited at 0.05 Å/s onto (a) MoO_3, (b) FDTS, and (c) CuI are shown. Most intense peaks are numbered and listed in Table S1 with the corresponding scattering vector q (cfr. eq 1) and potential peak assignments. The unit-cell parameters of the monoclinic[13] and triclinic[14] PbPc polymorph are listed in Table S2. This material is available free of charge via the Internet at http://pubs.acs.org.

AUTHOR INFORMATION

Corresponding Author

*E-mail: david.cheyns@imec.be. Phone: +32 16288139. Fax: +32 16 281097.

Notes

The authors declare no competing financial interest.

ACKNOWLEDGMENTS

K.V. acknowledges the Institute for the Promotion of Innovation through Science and Technology in Flanders (IWT-Vlaanderen) for financial support. F.S. acknowledges financial support from the DFG. A portion of this research was carried out at the Stanford Synchrotron Radiation Lightsource, a national user facility operated by Stanford University on behalf of the U.S. Department of Energy, Office of Basic Energy Sciences. K.V. acknowledges the Research Foundation Flanders (FWO) for a grant for a short stay abroad. The authors thank Stefan Mannsfeld for providing the WxDiff software package for GIXD data analysis.

REFERENCES

(1) Thompson, B. C.; Fréchet, J. M. J. *Angew. Chem., Int. Ed.* **2008**, *47*, 58−77.
(2) Liang, Y. Y.; Xu, Z.; Xia, J. B.; Tsai, S. T.; Li, G.; Ray, C.; Yu, L. P. *Adv. Mater.* **2010**, *22*, E135−E138.
(3) Service, R. F. *Science* **2011**, *332*, 293.
(4) Hadipour, A.; Cheyns, D.; Heremans, P.; Rand, B. P. *Adv. Energy Mater.* **2011**, *1*, 930−935.
(5) Sergeant, N. P.; Hadipour, A.; Niesen, B.; Cheyns, D.; Heremans, P.; Peumans, P.; Rand, B. P. *Adv. Mater.* **2012**, *24*, 728−732.
(6) Brabec, C. J.; Gowrisanker, S.; Halls, J. J. M.; Laird, D.; Jia, S.; Williams, S. P. *Adv. Mater.* **2010**, *22*, 3839−3856.
(7) Chang, C. Y.; Cheng, Y. J.; Hung, S. H.; Wu, J. S.; Kao, W. S.; Lee, C. H.; Hsu, C. S. *Adv. Mater.* **2012**, *24*, 549−553.
(8) Placencia, D.; Wang, W.; Gantz, J.; Jenkins, J. L.; Armstrong, N. R. *J. Phys. Chem. C* **2011**, *115*, 18873−18884.
(9) Verreet, B.; Müller, R.; Rand, B. P.; Vasseur, K.; Heremans, P. *Org. Electron.* **2011**, *12*, 2131−2139.
(10) Rand, B. P.; Cheyns, D.; Vasseur, K.; Giebink, N. C.; Mothy, S.; Yi, Y.; Beljonne, D.; Cornil, J.; Brédas, J.-L.; Genoe, J. *Adv. Funct. Mater.* **2012**, *22*, 2987−2995.
(11) Green, M. A.; Emery, K.; Hishikawa, Y.; Warta, W.; Dunlop, E. D. *Prog. Photovolt.: Res. Appl.* **2012**, *20*, 12−20.
(12) Cheyns, D.; Rand, B. P.; Heremans, P. *Appl. Phys. Lett.* **2010**, *97*, 033301.
(13) Claessens, C. G.; Hahn, U.; Torres, T. *Chem. Rec.* **2008**, *8*, 75−97.
(14) Gastonguay, L.; Veilleux, G.; Cote, R.; Saint-Jacques, R. G.; Dodelet, J. P. *Chem. Mater.* **1993**, *5*, 381−390.
(15) Yanagi, H.; Imamura, M.; Ashida, M. *J. Appl. Phys.* **1994**, *75*, 2061−2068.
(16) Mizuguchi, J.; Rihs, G.; Karfunkel, H. R. *J. Phys. Chem.* **1995**, *99*, 16217−16227.
(17) Yamaguchi, S.; Sasaki, J. *Chem. Phys. Lett.* **2000**, *323*, 35−42.
(18) Kera, S.; Fukagawa, H.; Kataoka, T.; Hosoumi, S.; Yamane, H.; Ueno, N. *Phys. Rev. B* **2007**, *75*, 121305.
(19) Norton, J. E.; Brédas, J.-L. *J. Chem. Phys.* **2008**, *128*, 034701.
(20) Hiller, W.; Strähle, J.; Kobel, W.; Hanack, M. *Z. Kristallogr.* **1982**, *159*, 173−183.
(21) Oka, K.; Okada, O.; Nukada, K. *Jpn. J. Appl. Phys.* **1992**, *31*, 2181−2184.
(22) Okada, O.; Oka, K.; Iijima, M. *Jpn. J. Appl. Phys.* **1993**, *32*, 3556−3560.
(23) Jennings, C. A.; Aroca, R.; Kovacs, G. J.; Hsaio, C. *J. Raman Spectrosc.* **1996**, *27*, 867−872.
(24) Ukei, K. *Acta Crystallogr., Sect. B* **1973**, *29*, 2290−2292.
(25) Iyechika, Y.; Yakushi, K.; Ikemoto, I.; Kuroda, H. *Acta Crystallogr., Sect. B* **1982**, *38*, 766−770.
(26) Collins, R. A.; Krier, A.; Abass, A. K. *Thin Solid Films* **1993**, *229*, 113−118.
(27) Campbell, D.; Collins, R. A. *Thin Solid Films* **1995**, *261*, 311−316.
(28) Campbell, D.; Collins, R. A. *Phys. Status Solidi a* **1995**, *152*, 431−442.
(29) Ottaviano, L.; Lozzi, L.; Phani, A. R.; Ciattoni, A.; Santucci, S.; Di Nardo, S. *Appl. Surf. Sci.* **1998**, *136*, 81.
(30) Sakata, M.; Sumimoto, M.; Gushima, M.; Fujimoto, H.; Matsuzaki, S. *Solid State Commun.* **2002**, *121*, 363−366.
(31) Miyamoto, A.; Nichogi, K.; Taomoto, A.; Nambu, T.; Murakami, M. *Thin Solid Films* **1995**, *256*, 64−67.
(32) Vasseur, K.; Rand, B. P.; Cheyns, D.; Froyen, L.; Heremans, P. *Chem. Mater.* **2011**, *23*, 886−895.
(33) Schreiber, F. *Phys. Status Solidi a* **2004**, *201*, 1037−1054.
(34) Sullivan, P.; Jones, T. S.; Ferguson, A. J.; Heutz, S. *Appl. Phys. Lett.* **2007**, *91*, 233114.
(35) Sakurai, T.; Fukasawa, R.; Saito, K.; Akimoto, K. *Org. Electron.* **2007**, *8*, 702−708.
(36) Virkar, A. A.; Mannsfeld, S.; Bao, Z.; Stingelin, N. *Adv. Mater.* **2010**, *22*, 3857−3875.
(37) Lassiter, B. E.; Lunt, R. R.; Renshaw, C. K.; Forrest, S. R. *Opt. Express* **2010**, *18*, A444−A450.
(38) Perlich, J.; Memesa, M.; Diethert, A.; Metwalli, E.; Wang, W.; Roth, S. V.; Timmann, A.; Gutmann, J. S.; Müller-Buschbaum, P. *ChemPhysChem* **2009**, *10*, 799−805.
(39) Dai, J.; Jiang, X.; Wang, H.; Yan, D. *Appl. Phys. Lett.* **2007**, *91*, 253503.
(40) Hiramoto, M.; Kitada, K.; Iketaki, K.; Kaji, T. *Appl. Phys. Lett.* **2011**, *98*, 023302.
(41) Sakurai, T.; Ohashi, T.; Kitazume, H.; Kubota, M.; Suemasu, T.; Akimoto, K. *Org. Electron.* **2011**, *12*, 966−973.
(42) Zhao, W.; Mudrick, J. P.; Zheng, Y.; Hammond, W. T.; Yang, Y.; Xue, J. *Org. Electron.* **2012**, *13*, 129−135.
(43) Shim, H.-S.; Kim, H. J.; Kim, J. W.; Kim, S.-Y.; Jeong, W.-I.; Kim, T.-M.; Kim, J.-J. *J. Mater. Chem.* **2012**, *22*, 9077−9081.
(44) Kim, H. J.; Shim, H.-S.; Kim, J. W.; Lee, H. H.; Kim, J.-J. *Appl. Phys. Lett.* **2012**, *100*, 263303.
(45) Cheng, C. H.; Wang, J.; Du, G. T.; Shi, S. H.; Du, Z. J.; Fan, Z. Q.; Bian, J. M.; Wang, M. S. *Appl. Phys. Lett.* **2010**, *97*, 083305.
(46) Vasseur, K.; Rand, B. P.; Cheyns, D.; Temst, K.; Froyen, L.; Heremans, P. *J. Phys. Chem. Lett.* **2012**, *3*, 2395−2400.
(47) Khodabakhsh, S.; Sanderson, B. M.; Nelson, J.; Jones, T. S. *Adv. Funct. Mater.* **2006**, *16*, 95−100.

(48) Sharma, A.; Haldi, A.; Hotchkiss, P. J.; Marder, S. R.; Kippelen, B. *J. Appl. Phys.* **2009**, *105*, 074511.
(49) Bulliard, X.; Ihn, S.-G.; Yun, S.; Kim, Y.; Choi, D.; Choi, J.-Y.; Kim, M.; Sim, M.; Park, J.-H.; Choi, W.; Cho, K. *Adv. Funct. Mater.* **2010**, *20*, 4381−4387.
(50) Beaumont, N.; Hancox, I.; Sullivan, P.; Hatton, R. A.; Jones, T. S. *Energy Environ. Sci.* **2011**, *4*, 1708−1711.
(51) Schreiber, F. *Prog. Surf. Sci.* **2000**, *65*, 151−256.
(52) Hinderhofer, A.; Schreiber, F. *Chem. Phys. Chem.* **2012**, *13*, 628−643.
(53) Kim, D. Y.; Sarasqueta, G.; So, F. *Sol. Energy Mater. Sol. Cells* **2009**, *93*, 1452−1456.
(54) Hancox, I.; Chauhan, K. V.; Sullivan, P.; Hatton, R. A.; Moshar, A.; Mulcahy, C. P. A.; Jones, T. S. *Energy Environ. Sci* **2010**, *3*, 107−110.
(55) Li, L.; Tang, Q.; Li, H.; Yang, S.; Hu, W.; Song, Y.; Shuai, A.; Xu, W.; Liu, Y.; Zhu, D. *Adv. Mater.* **2007**, *19*, 2613−2617.
(56) Li, L.; Hu, W.; Fuchs, H.; Chi, L. *Adv. Energy Mater.* **2011**, *1*, 188−193.
(57) Opitz, A.; Wagner, J.; Brütting, W.; Hinderhofer, A.; Schreiber, F. *Phys. Staus Solidi a* **2009**, *12*, 2683−2694.
(58) Wagner, J.; Gruber, M.; Hinderhofer, A.; Wilke, A.; Bröker, B.; Frisch, J.; Amsalem, P.; Vollmer, A.; Opitz, A.; Koch, N.; Schreiber, F.; Brütting, W. *Adv. Funct. Mater.* **2010**, *20*, 4295−4303.
(59) Ruderer, M. A.; Prams, S. M.; Rawolle, M.; Zhong, Q.; Perlich, J.; Roth, S. V.; Müller-Buschbaum, P. *J. Phys. Chem. B* **2010**, *114*, 15451−15458.
(60) Perlich, J.; Rubeck, J.; Botta, S.; Gehrke, R.; Roth, S. V.; Ruderer, M. A.; Prams, S. M.; Rawolle, M.; Zhong, Q.; Körstgens, V.; Müller-Buschbaum, P. *Rev. Sci. Instrum.* **2010**, *81*, 105105.
(61) Kohn, P.; Rong, Z.; Scherer, K. H.; Sepe, A.; Sommer, M.; Müller-Buschbaum, P.; Friend, R. H.; Steiner, U.; Hüttner, S. *Macromolecules* **2013**, *46*, 4002−4013.
(62) Khan, H. U.; Li, R.; Ren, Y.; Chen, L.; Payne, M. M.; Bhansali, U. S.; Smilgies, D. M.; Anthony, J. E.; Amassian, A. *ACS Appl. Mater. Interfaces* **2013**, *5*, 2325−2330.
(63) Mannsfeld, S. C. B.; Tang, M. L.; Bao, Z. *Adv. Mater.* **2011**, *23*, 127−131.
(64) Jimison, L. H. Understanding Microstructure and Charge Transport in Semicrystalline Polythiophenes. PhD Dissertation [Online], Stanford University, Stanford, CA, March 2011. http://purl.stanford.edu/rk242cd0160 (accessed Aug 1, 2013).
(65) Ritley, K. A.; Krause, B.; Schreiber, F.; Dosch, H. *Rev. Sci. Instrum.* **2001**, *72*, 1453−1457.
(66) Krause, B.; Schreiber, F.; Dosch, H.; Pimpinelli, A.; Seeck, O. H. *Europhys. Lett.* **2004**, *65*, 372−378.
(67) Kowarik, S.; Gerlach, A.; Sellner, S.; Schreiber, F.; Cavalcanti, L.; Konovalov, O. *Phys. Rev. Lett.* **2006**, *96*, 125504.
(68) Hosokai, T.; Gerlach, A.; Hinderhofer, A.; Frank, C.; Ligorio, G.; Heinemeyer, U.; Vorobiev, A.; Schreiber, F. *Appl. Phys. Lett.* **2010**, *97*, 063301.
(69) Baker, J. L.; Jimison, L. H.; Mannsfeld, S.; Volkman, S.; Yin, S.; Subramanian, V.; Salleo, A.; Alivisatos, A. P.; Toney, M. F. *Langmuir* **2010**, *26*, 9146−9151.
(70) Mattheus, C. C.; Michaelis, W.; Kelting, C.; Durfee, W. S.; Wöhrle, D.; Schlettwein, D. *Synth. Met.* **2004**, *146*, 335−339.
(71) Alonso, M. I.; Garriga, M.; Karl, N.; Ossó, J. O.; Schreiber, F. *Org. Electron.* **2002**, *3*, 23−31.
(72) Kowarik, S.; Broch, K.; Hinderhofer, A.; Schwartzberg, J.; Ossó, J. O.; Kilcoyne, D.; Schreiber, F.; Leone, S. R. *J. Phys. Chem. C* **2010**, *114*, 13061−13067.
(73) Yonehara, H.; Ogawa, K.; Etori, H.; Pac, C. *Langmuir* **2002**, *18*, 7557−7563.
(74) Ossó, J. O.; Schreiber, F.; Alonso, M. I.; Garriga, M.; Barrena, E.; Dosch, H. *Org. Electron.* **2004**, *5*, 135−140.
(75) Hoshi, H.; Fang, S.; Maruyama, Y. *J. Appl. Phys.* **1993**, *73*, 3111.
(76) Gerlach, A.; Schreiber, F.; Sellner, S.; Dosch, H.; Vartanyants, I. A.; Cowie, B. C. C.; Lee, T.-L.; Zegenhagen, J. *Phys. Rev. B* **2005**, *71*, 205425.
(77) Gerlach, A.; Hosokai, T.; Kera, S.; Hofmann, O. T.; Zojer, E.; Zegenhagen, J.; Schreiber, F. *Phys. Rev. Lett.* **2011**, *106*, 156102.
(78) Heinemeyer, U.; Broch, K.; Hinderhofer, A.; Kytka, M.; Scholz, R.; Gerlach, A.; Schreiber, F. *Phys. Rev. Lett.* **2010**, *104*, 257401.
(79) Cruickshank, A. C.; Dotzler, C. J.; Din, S.; Heutz, S.; Toney, M. F.; Ryan, M. P. *J. Am. Chem. Soc.* **2012**, *134*, 14302−14305.
(80) Kline, R. J.; McGehee, M. D.; Toney, M. F. *Nat. Mater.* **2006**, *5*, 222−228.
(81) Kowarik, S.; Gerlach, A.; Schreiber, F. *J. Phys.: Condens. Matter* **2008**, *20*, 184005.
(82) Cheyns, D.; Rand, B. P.; Heremans, P. *Appl. Phys. Lett.* **2010**, *97*, 33301.
(83) Lunt, R. R.; Benziger, J. B.; Forrest, S. R. *Adv. Mater.* **2010**, *22*, 1233−1236.
(84) Cheyns, D.; Poortmans, J.; Heremans, P.; Deibel, C.; Verlaak, S.; Rand, B P; Genoe, J. *Phys. Rev. B* **2008**, *77*, 165332.